Supplemental Material: Tunable three-body loss in a Rydberg nonlinear medium

D. P. Ornelas-Huerta,[1] Przemyslaw Bienias,[1,2] Alexander N. Craddock,[1] Michael J. Gullans,[1,2,3] Andrew J. Hachtel,[1] Marcin Kalinowski,[1,4] Mary E. Lyon,[1] Alexey V. Gorshkov,[1,2] Steven L. Rolston,[1] and J. V. Porto[1]

[1] *Joint Quantum Institute, NIST/University of Maryland, College Park, Maryland 20742 USA*
[2] *Joint Center for Quantum Information and Computer Science, NIST/University of Maryland, College Park, Maryland 20742 USA*
[3] *Department of Physics, Princeton University, Princeton, New Jersey 08544 USA*
[4] *Faculty of Physics, University of Warsaw, Pasteura 5, 02-093 Warsaw, Poland*

(Dated: January 8, 2021)

In this Supplemental Material, we expand upon experimental and theoretical aspects of this work. In Sec. I, we describe experimental methods for atom preparation, two-photon excitation, light collection, and correlation function measurements. In Sec. II, we present the Fermi's Golden Rule calculation and some associated analytical expressions.

I. EXPERIMENTAL METHODS

A. Atom preparation

We load ^{87}Rb atoms into a magneto-optical trap from background vapor for 250 ms. We use a Λ-gray molasses [S1] scheme on the D2 transition to cool the atoms down to 10 μK, and confine them in an optical dipole trap made of 1003-nm light. The trapped atomic cloud has dimensions $\sigma_r = 20 \pm 2$ μm in the radial direction, and an axial extension along the probe propagation of $\sigma_z = 42 \pm 2$ μm. The resulting optical depth is OD $= 37 \pm 4$ with $\approx 10^5$ atoms. The dipole trap consists of three beams that intersect at the probe beam focus. Two of the beams form a $\approx \pm 11^\circ$ crossed trap with respect to the z-axis (along the probe direction), while a third elliptical shaped beam travels in the y-axis; all beams lie on the same (z-y) plane. We optically pump the atoms into the stretched state $\left|5\mathrm{S}_{1/2}, F = 2, m_F = 2\right\rangle$, using σ_+-polarized light blue-detuned from the $F = 2$ to $F' = 2$, D1 transition.

B. Two-photon excitation

We couple the ground and Rydberg state with a two-photon transition. A 780-nm weak probe field addresses the transition from the ground state, $|G\rangle = \left|5\mathrm{S}_{1/2}, F = 2, m_F = 2\right\rangle$ to the intermediate state, $|P\rangle = \left|5\mathrm{P}_{3/2}, F = 3, m_F = 3\right\rangle$; a strong control field addresses the transition from the intermediate state to the Rydberg state, $|S\rangle = \left|82\mathrm{S}_{1/2}, J = 1/2, m_J = 1/2\right\rangle$ with a wavelength of 479 nm.

The probe and control lasers are frequency stabilized via a Pound-Drever Hall lock scheme using an ultra-low expansion (ULE) cavity with a linewidth < 10 kHz. We use the probe light that has been transmitted and filtered by the ULE cavity to reduce phase noise during the two-photon excitation [S2].

The measured linewidth for both the $|G\rangle$-$|P\rangle$ and $|P\rangle$-$|S\rangle$ transitions are $\Gamma/(2\pi) = 7 \pm 1$ MHz and $\gamma/(2\pi) = 0.4 \pm 0.1$ MHz, respectively. The latter is broadened beyond the natural linewidth by various dephasing mechanisms e.g. differential light shifts and Doppler broadening.

We focus the probe beam down to a $1/e^2$ waist of $w_p \approx 3.3$ μm to ensure the system is effectively one dimensional ($w_p < r_b$), where the blockade radius r_b ranges from 7 to 10 μm. The control beam is counter-propagating to the probe and focused to a beam waist of $w_c \approx 19$ μm. The larger beam waist provides an approximately uniform control field across the probe area.

We interrogate the atoms continuously for 100 ms before we repeat the loading and cooling cycle, resulting in an experimental duty-cycle of $\simeq 0.13$.

C. Light collection and filtering

After exiting the chamber, the probe light passes through a polarization beam splitter (PBS), and a narrow 1-nm spectral filter (Alluxa 780-1 OD6 [S3]) to reduce the amount of background light reaching the detectors, due to e.g. leakage of room light and broad-band fluorescence from the control laser. The probe is equally split in three using an arrangement of half-waveplates and two PBS, and is then coupled to multi-mode fibers and sent to single-photon avalanche photo detectors (SPAD) Excelitas SPCM-780-13 [S3]).

D. Correlation measurements

The detection events from the SPADs are recorded as time-stamps by a triggered time-tagger device (Roithner TTM8000 [S3]). We calculate the second-order correlation function as,

$$g^{(2)}(\tau) = \frac{N_{12}(\tau)}{\frac{1}{8}\sum_{m=1}^{4} N_{12}(\tau \pm mT)}, \tag{S1}$$

where $N_{12}(\tau)$ are the measured coincidences as a function of the relative time τ of detection between each SPAD pair accumulated for 1500 experimental cycles. The normalization is done by counting the coincidence events for $\tau + mT$, where $T = 100$ μs and m is an integer number. The coincidences for large τ are given by $N_{12}(\tau \pm mT) = N_1 N_2 \Delta\tau / T_{\text{exp}}$. Here, $\Delta\tau$ is the binning time (which corresponds to 20 ns in the experimental data shown in the main text), and N_j is the average detection counts for the j-th SPAD in a time-bin $\Delta\tau$, and T_{exp}=100 ms is the total experimental time. This normalization allows to cancel slow experimental drifts with time scales longer than T, that could be imprinted in the correlation measurements.

The third order correlation function is calculated as,

$$g^{(3)}(\tau_1, \tau_2) = \frac{N_{123}(\tau_1, \tau_2)}{\frac{1}{56}\sum_{m=1,n=1,m\neq n}^{4} N_{123}(\tau_1 \pm mT, \tau_2 \pm nT)}, \tag{S2}$$

where $N_{123}(\tau_1, \tau_2)$ are the measured coincidences as a function of two relative times τ_1 and τ_2, and is given by $N_{123}(\tau_1, \tau_2) = N_1 N_2 N_3 (\Delta\tau/T)^2$. For the normalization of $g^{(3)}(\tau_1, \tau_2)$, we ignore the indexes where $m = n$, since $g^{(3)}(\tau, \tau) = g^{(2)}(0)$.

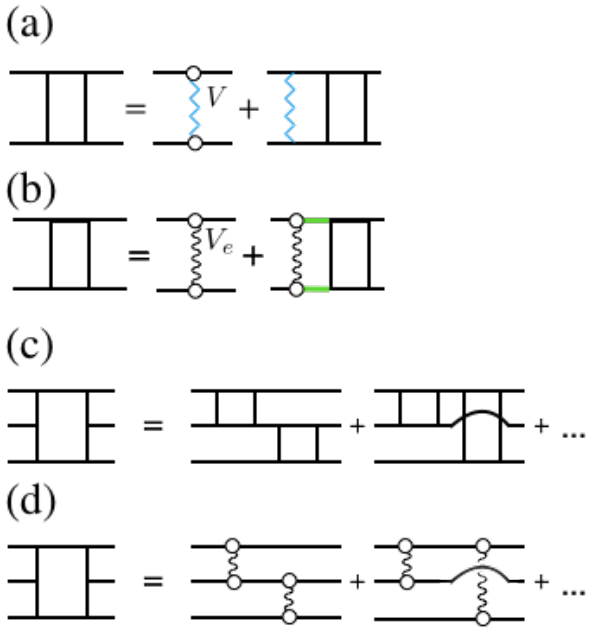

FIG. S1. T-matrix representation of the two-body (a-b) and three-body (c-d) problem. Wiggly black line depicts V_e, whereas polygonal blue line depicts V. See main text for the details.

II. FERMI'S GOLDEN RULE CALCULATION

Here, we present the Fermi's Golden Rule calculation described in the main text. For Rydberg polaritons, only interactions between Rydberg levels are non-negligible. Therefore, in the basis of atomic and photonic states, only the T-matrix between Rydberg states is non-zero.

The Lippmann-Schwinger equation for the two-body T-matrix is shown in Fig. S1(a), where in all diagrams henceforth the rectangles denote two- and three-body T-matrices.

From Ref. [S4], we know that the T-matrix equation for the two-body scattering problem can be rewritten using effective interactions V_e, see Fig. S1(b). This approach has the advantage that effective interaction is non-divergent in the relative distance between the polaritons, in contrast to the initial T-matrix equation written in terms of V. Note that, in this case, the two-body propagator (depicted as two green horizontal lines between V_e and T) includes only the poles that have a nontrivial momentum dependence (the momentum-independent spin-wave contribution $\bar{\chi}$ to the two-body propagator χ is taken into account in V_e).

The equations for the three-body T-matrix are called Faddeev equations. The three-body T-matrix is written as an infinite sum of diagrams involving two-body T-matrices, Fig. S1(c), in a mathematically consistent way.

To estimate β, for $\varphi < 1$, we can consider only diagrams contributing in the leading second order in $V_e \sim \varphi$, see Fig. S1(d). In other words, we replace the two-body T-matrix by the first term V_e on the right-hand side of the two-body Lippman-Schwinger equation in Fig. S1(b).

For the calculation of β, we are interested in the T-matrix elements between incoming dark polaritons and outgoing lossy polaritons. For this purpose, it is useful to consider the T-matrix in the polaritonic basis; and, in the expressions for β, we include only the connected diagrams with the additional condition that they do not end in the three dark polaritons. Finally, as explained in the main text, we find that the leading contribution to the Fermi's Golden Rule scattering rate β comes from the scattering to the DDU channel–the corresponding diagrams are shown in Fig. 4 of the main text.

A. Additional analytical expressions

Here we present expressions for the single-body propagator and for ω_+, as well the expressions used to justify that the resonance in the Fermi's Golden Rule integral caused by the density of states can be neglected.

For the sake of brevity, all the expressions in this subsection are presented for $\gamma_s \ll \Gamma$. In order to arrive at more general expressions, one should replace Δ by $\tilde{\Delta} = \Delta - i\gamma_s/2$.

The single-body propagator $G_{ss}[k, \omega]$, used in the main

text, is given by

$$\frac{(\omega - ck)(\Delta + \Delta_s + \omega) - g^2}{(\Delta_s + \omega)((\omega - ck)(\Delta + \Delta_s + \omega) - g^2) + \frac{1}{4}\Omega^2(ck - \omega)}. \tag{S3}$$

while ω_+ is given by

$$\omega_+ = \frac{1}{2}\left(-\Delta + \sqrt{\Delta^2 + 2\Delta\Delta_s + \Delta_s^2 + \Omega^2} + \Delta_s\right). \tag{S4}$$

Next we discuss the cancellation of the resonance from the density of states with a zero from $1/\bar{\chi}$ within the Fermi's Golden Rule calculation. Expression for $1/\bar{\chi}[-\omega_+]$ takes the form

$$\frac{\left(-3\Delta + \sqrt{(\Delta + \Delta_s)^2 + \Omega^2} - 3\Delta_s\right)\left(-3\Delta^2 + 3\Delta\sqrt{(\Delta + \Delta_s)^2 + \Omega^2} + 3\Delta_s\sqrt{(\Delta + \Delta_s)^2 + \Omega^2} - 10\Delta\Delta_s - 5\Delta_s^2 + \frac{3\Omega^2}{2}\right)}{2\left(-8\Delta^2 + 4\Delta\sqrt{(\Delta + \Delta_s)^2 + \Omega^2} + 3\Delta_s\sqrt{(\Delta + \Delta_s)^2 + \Omega^2} - 13\Delta\Delta_s - 5\Delta_s^2 + \frac{\Omega^2}{2}\right)}, \tag{S5}$$

which, for $\Delta_s \to 0$, equals

$$\frac{\left(\sqrt{\Delta^2 + \Omega^2} - 3\Delta\right)\left(3\Delta\sqrt{\Delta^2 + \Omega^2} - 3\Delta^2 + \frac{3\Omega^2}{2}\right)}{2\left(4\Delta\sqrt{\Delta^2 + \Omega^2} - 8\Delta^2 + \frac{\Omega^2}{2}\right)}. \tag{S6}$$

The density of states is proportional to $1/v_g(-2\omega_+)$, which, for $g \gg \Omega, |\Delta_s|, |\Delta|$, is equal to

$$\frac{g^2\left(\Delta - \sqrt{\Delta^2 + 2\Delta\Delta_s + \Delta_s^2 + \Omega^2}\right)^2 + \frac{g^2\Omega^2}{4}}{c\left(3\Delta^2 - 3\Delta\sqrt{\Delta^2 + 2\Delta\Delta_s + \Delta_s^2 + \Omega^2} + 2\Delta\Delta_s + \Delta_s^2 + \frac{3\Omega^2}{4}\right)^2}, \tag{S7}$$

which, for $\Delta_s \to 0$, in turn equals

$$\frac{g^2\left(-2\Delta\sqrt{\Delta^2 + \Omega^2} + 2\Delta^2 + \frac{5\Omega^2}{4}\right)}{9c\left(-\Delta\sqrt{\Delta^2 + \Omega^2} + \Delta^2 + \frac{\Omega^2}{4}\right)^2}. \tag{S8}$$

The divergence from the denominator of Eq. (S8) at $\Delta \approx \Omega/2\sqrt{2}$ cancels with the square of $\left(\sqrt{\Delta^2 + \Omega^2} - 3\Delta\right)$ from the numerator of Eq. (S6). For nonzero Δ_s, this cancellation is approximate. Furthermore, the dependence of r_b on $\bar{\chi}$ also leads to a residual divergence. Both effects, however, are not significant due the non-negligible imaginary component of the detunings.

[S1] S. Rosi, A. Burchianti, S. Conclave, D. S. Naik, G. Roati, C. Fort, and F. Minardi, Scientific Reports **8**, 1301 (2018).

[S2] S. de Léséleuc, D. Barredo, V. Lienhard, A. Browaeys, and T. Lahaye, Phys. Rev. A **97**, 053803 (2018).

[S3] The identification of commercial products in this paper does not imply recommendation or endorsement by the National Institute of Standards and Technology nor does it imply that the items identified are necessarily the best available for the purpose.

[S4] P. Bienias, S. Choi, O. Firstenberg, M. F. Maghrebi, M. Gullans, M. D. Lukin, A. V. Gorshkov, and H. P. Büchler, Phys. Rev. A **90**, 053804 (2014).